



Insight into Structural and Optical Properties of Pristine and Sr²⁺ Doped La₂NiMnO₆

Javed Ahmad^{*1}, Shoaib Hassan¹, Jamshaid Alam Khan¹, Umair Nissar¹,
and Hammad Abbas¹

¹Department of Physics, Bahauddin Zakariya University, Multan 60800, Pakistan

Abstract: Double perovskites oxide (DPO) multiferroics La_{2-x}Sr_xNiMnO₆ (x=0.0, 0.1, 0.2, 0.4, 0.6) are synthesized by sol-gel technique. The structural, optical and electrical (both DC and AC) properties of La_{2-x}Sr_xNiMnO₆ have been investigated by XRD and FTIR spectroscopy and two-probe resistivity and dielectric measurements as a function of temperature, respectively. The effect of doping of Strontium at A-site in double perovskites is discussed. XRD has revealed the formation of monoclinic structure of La_{2-x}Sr_xNiMnO₆ with space group $P2_1/n$ for x=0.0 and $P2_1$ for x=0.1, 0.2, 0.4, 0.6. The average crystallite size has been calculated to be in the range 31 to 46 nm as determined by Debye Scherrer equation. Infrared active optical phonons observed from reflectivity spectra have been analysed fitting the theoretical oscillators using Lorentz oscillator model. We have observed several well-resolved phonon modes in La_{2-x}Sr_xNiMnO₆ with increasing dopant concentration. Activation energy calculated using Arrhenius Plot is in the range of 0.31 to 0.18 eV, confirming the semiconducting nature of all samples. The dielectric constant and tangent loss as a function of temperature and frequency are also discussed for these multiferroics.

Keywords: X-ray Diffraction; Fourier Transform Infrared Spectroscopy (FTIR); Optical Phonons; Electrical Resistivity

1. INTRODUCTION

Double perovskite La₂NiMnO₆ (LNMO) is an alluring compound, which has extended range of applications in modern electronic devices such as resonators, piezoelectric and pyro-electric transducers and capacitors etc. [1]. Some of the perovskites have a large range of applications in magnetoelectric capacitors [2, 3], solar cells, solid state thermoelectric Peltier coolers [4], spin filtering tunnel junction [5, 6] etc. By virtue of their enriched physics and technological applications in spintronic devices [7], the oxides of double perovskites have obtained foremost significance and thus been investigated by several researchers.

Perovskites oxides having general formula ABO₃ belongs to an important class of materials as these materials have fascinating physical properties, for instance multiferrocity [8], superconductivity [9] and metal insulator transition [10]. When the B-site cation in ABO₃ is replaced by two cations

B' and B'', we obtain a complex structure of perovskites A₂B'B''O₆ which is known as double perovskites. In A₂B'B''O₆, B' and B'' represent rare earth and alkaline earth metals, respectively. While B' and B'' are the two different cations on B-site they represent the transition metals. The difference of size and charge, which may be large or small between two B-site cations (B' and B'') is responsible for the ordered or disordered arrangements of the two cations [11]. Several DPOs in which B-site cations are referred to as ferri/ferromagnetic exhibit the magneto-resistive behaviour [12]. Double perovskites La₂NiMnO₆ exhibits (FM) ferromagnetic and insulating behaviour at room temperature [13]. For LNMO, Ni-O-Ni and Mn-O-Mn configurations resulted due to the anti-site disorder which is responsible for (AFM) antiferromagnetic interactions, depending upon superexchange rules [14]. Ferromagnetic LNMO shows the ordered double perovskite structure, in which MnO₆ and NiO₆ octahedra have rock-salt configuration [15]. Recently the study

of magnetic properties of $\text{La}_2\text{NiMnO}_6$ DPO has received tremendous research interest, particularly in the context of, e.g., cation oxidation state ($\text{Ni}^{2+}/\text{Mn}^{4+}$ or $\text{Ni}^{3+}/\text{Mn}^{3+}$) and the atomic Ni/Mn B-site ordering [16]. When La on A-site is substituted by some other rare-earth cation in LNMO compounds; the bond angle and bond length between Ni-O-Mn may experience some changes in the magnetic configurations [17-19]. Although thermodynamically, magnetite and double perovskites are known as most stable compounds, however, it has been revealed also that presence of anti-site disorder is appeared by interaction between A, B' and B'' and may weaken the stability [20]. To study role of A site substitution on the site ordering, it would be interesting to substitute A site trivalent La^{3+} by a divalent cation such as Sr^{2+} in $\text{La}_{2-x}\text{Sr}_x\text{NiMnO}_6$ keeping magnetically active B site intact. The choice of Sr is due to the fact that the ionic radii of Sr^{2+} is larger than that of La^{3+} and that the stability of crystal structure is enhanced which is evident by tolerance factor calculations as by increasing concentration of Sr, the tolerance factor reaches to one [1].

In this research work, the double perovskite $\text{La}_{2-x}\text{Sr}_x\text{NiMnO}_6$ for ($x=0.0, 0.1, 0.2, 0.4, 0.6$) were prepared successfully by sol-gel auto combustion method. The synthesized materials were characterised by XRD, FTIR and temperature-dependent electrical resistivity and dielectric measurement and results are discussed to comprehend physics of the multiferroics.

2. MATERIALS AND METHODS

Double perovskites $\text{La}_{2-x}\text{Sr}_x\text{NiMnO}_6$ ($x = 0.0, 0.1, 0.2, 0.4, 0.6$) were synthesized by sol-gel auto combustion method. The powder so obtained was sintered at 1000°C for about 6 hours [21]. The structure and single phase of the crystalline samples were determined using a latest X-ray diffractometer (D8 Bruker) equipped with Cu-K α ($\lambda=1.54\text{\AA}$) radiation source. Infrared reflectivity spectra have been recorded at room temperature in the near-normal incidence configuration using Fourier transform infrared spectrometer (Vertex 80v by Bruker) in the frequency range $30\text{-}7500\text{ cm}^{-1}$, which has been covered using various beam splitter detector combinations; i.e., KBr-DLaTGS beam splitter-detector combination for $370\text{-}7500$

cm^{-1} and Mylar $6\mu\text{m}$ -DLATGS for $30\text{-}680\text{ cm}^{-1}$. The gold film has been used as a reference; its reflectivity spectrum has been measured in the same optical alignment and spectral parameters fixed for that of measuring the sample reflectivity. Then the sample reflectivity spectrum has been divided with that of the reference spectrum in order to nullify the spectral response due to the spectrometer. This absolute reflectivity has been analysed using Lorentz oscillator model in order to account for the various optical phonon modes. The temperature dependent electrical resistivity measurements up to 20V were taken by two-point-probe method with a Keithley source meter (No. 2400). The dielectric constant and tangent loss have been measured in frequency range $20\text{Hz}\text{-}1\text{MHz}$ by using a LCR meter (GW Instek 8101). Furthermore, transport properties, i.e., resistivity and dielectric (both AC and DC), are analysed for temperatures ranging from 303 to 473 K .

3. RESULTS AND DISCUSSIONS

3.1 X-ray Diffraction

The structure and phase of the crystalline sample $\text{La}_{2-x}\text{Sr}_x\text{NiMnO}_6$ where ($x= 0.0, 0.1, 0.2, 0.4, 0.6$) have been observed by utilizing XRD technique. Rietveld refinement and Pseudo Voigt function have been utilised to analyse the XRD pattern fitted using "JANA2006" software. It is found that $\text{La}_2\text{NiMnO}_6$ consists of two space groups; (1) monoclinic $P2_1/n$ and (2) orthorhombic $Pbnm$. The first one is due to the ordered distribution of B-site atoms ($\text{Ni}^{2+}, \text{Mn}^{4+}$) while the second one is due to the disordered distribution of B-site atoms ($\text{Ni}^{3+}, \text{Mn}^{3+}$) [17].

Further, Rietveld Refinement and best-fitted data suggest that all the samples of double perovskite $\text{La}_{2-x}\text{Sr}_x\text{NiMnO}_6$ series have monoclinic structure ($P2_1$) and there is slight increase in lattice parameters from $\text{La}_2\text{NiMnO}_6$ to $\text{La}_{2-x}\text{Sr}_x\text{NiMnO}_6$ as shown in Table 1. The major peak at $2\theta=32.81^\circ$ was slightly shifted as we increased doping concentration ($x= 0.0, 0.1, 0.2, 0.4, 0.6$) and it may be due to the large ionic size of Strontium. The increase in cell volume/lattice parameters also seems to be due to the substitution of Strontium (Sr^{2+}) with large ionic radii in place of the Lanthanum (La^{3+}) having comparatively small ionic radii. By the process of

Rietveld Refinement, the cells parameters, factor of goodness Rwp and Rp calculated are tabulated in Table 1.

Crystalline sizes of $\text{La}_{2-x}\text{Sr}_x\text{NiMnO}_6$ where ($x=0.0, 0.1, 0.2, 0.4, 0.6$) are calculated by well-known Debye-Scherrer formula [22]:

$$D = \frac{k.\lambda}{\beta.\cos\theta} \quad (1)$$

Where $k = 0.9$ is the shape factor, $\lambda = 1.5405 \text{ \AA}$ is the wavelength, θ is the Bragg's angle, β is the Full width at half maximum. The trend of crystalline sizes are decreasing that can be seen in Table 1 and from the literature it is notified that as we doped "Sr" in rare earth at A-site the crystalline size of sample decreases with an increase in concentration [1].

3.2 Infrared Reflectivity

In Fig. 2, the reflectivity spectra of $\text{La}_{2-x}\text{Sr}_x\text{NiMnO}_6$ ($x=0.0, 0.1, 0.2, 0.4, 0.6$) are shown. We find that there are 4-major peaks or active IR bands. In case of $\text{La}_2\text{NiMnO}_6$, structure is monoclinic and according to group theory, 24 Raman active modes ($12 A_g + 12 B_g$) and 33 infrared (IR) active modes are observed for monoclinic structure. In all samples, 4-major active phonons were observed, having small distortion, responsible for lowering the symmetry. We observed 12 instead of 33 phonons in $\text{La}_{2-x}\text{Sr}_x\text{NiMnO}_6$.

The Lorentz Oscillator Model was used to analyse the IR spectra by fitting the model. This model is related to the dielectric function and optical reflectivity spectra through Fresnel's Formula:

$$R(\omega) = \left| \frac{\sqrt{\varepsilon(\omega)} - 1}{\sqrt{\varepsilon(\omega)} + 1} \right|^2 \quad (2)$$

Frequency-dependent dielectric function $\varepsilon(\omega)$ can be measured by IR active phonon modes. The dielectric function is:

$$\varepsilon(\omega) = \varepsilon_\infty + \sum_j \frac{\Sigma_j \omega_{TO(j)}^2 S_j}{\omega_{TO(j)} - \omega^2 - i\omega\gamma_j} \quad (3)$$

In this equation, the " ε_∞ " represents dielectric constant at very high frequency, " $\omega_{TO(j)}$ " is transverse frequency, " γ_j " is damping factor and " S_j " is oscillation strength of the j^{th} phonon.

The best-fitted parameters are shown in Tables 2, 3 & 4. The vibrational oscillation width of related phonons are determined by the damping factor " γ " shown in Table 3 and the amplitude of related phonons represented by the Oscillator strength " S " is shown in Table 4. The reflectivity spectra of $\text{La}_{2-x}\text{Sr}_x\text{NiMnO}_6$ ($x=0.0, 0.1, 0.2, 0.4, 0.6$) show that shifting of phonon modes occur as we increase the concentration of strontium, in the region of ($\leq 200 \text{ cm}^{-1}$). This shift in phonon resonant frequency may be due to two components, i.e., force constant and mass substitution effects;

$$\omega = \sqrt{D/\mu} \quad (4)$$

In the above equation of harmonic oscillator, " D " is force constant and it usually depends upon lattice parameters, bond angle and bond length. " μ " is the reduced mass that is linked to phonon modes. The mass substitution is obtained from the increasing concentration of "Sr" at A-site, so ions of rare earth metal should lower the reduced mass and as a result the ' ω ' will increase [23].

By addition of "Sr" in rare earth, it would decrease the mean mass of rare earth. As mass of "Sr" ($m_{\text{Sr}} = 87.62 \text{ amu}$) is lower as compared to ($m_{\text{La}} = 138.9 \text{ amu}$) mass of Lanthanum. Phonon frequency shifting is observed due to reduced mass, with participation of vibrations of transition metals and rare earth ions (La-Sr). Since mass of "Sr" is smaller than that of "La", as a harmonic oscillator, frequency of phonons increases. As far assignment of observed modes, the IR reflectivity spectra consist of three types of modes, namely, external mode (lower frequency mode), bending mode (intermediate frequency mode), and stretching mode (high frequency mode). Above 200 cm^{-1} , (bending mode) intermediate mode observed due to the B-site ions movement against (MnO_6) oxygen vibrations. Above 500 cm^{-1} , IR phonon modes are usually related to the octahedral (Ni/MnO_6) stretching [24].

As it is predicted that the gradual substitution of Sr^{2+} over La^{3+} can be related to the changes in oscillation modes observed below 200 cm^{-1} , which may be due to the reduction of mass at this site. There is only one phonon (ω_{TO1}) found at $155, 151, 146, 159, \text{ and } 160 \text{ cm}^{-1}$ for ($x=0.0, 0.1, 0.2, 0.4, 0.6$) respectively below 200 cm^{-1} , which shows

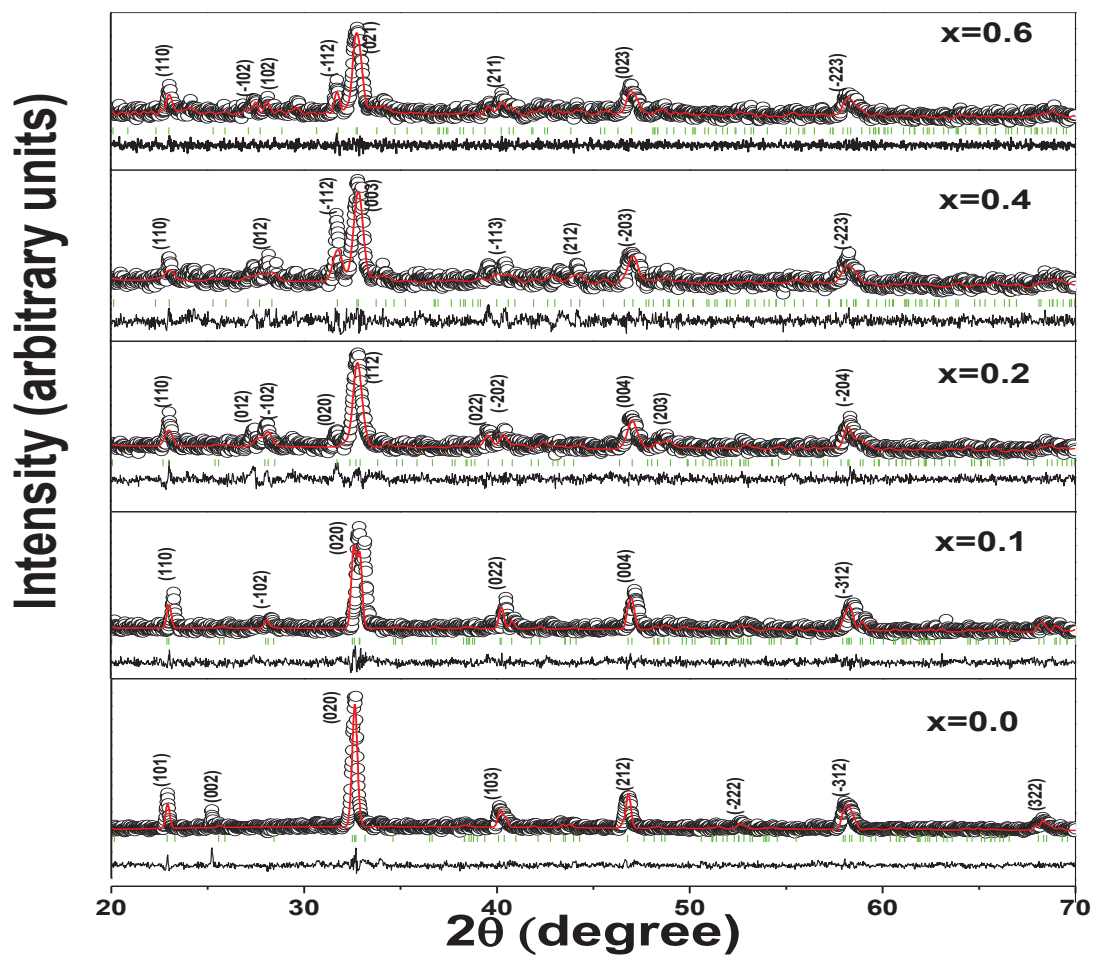


Fig. 1. XRD patterns of $\text{La}_{2-x}\text{Sr}_x\text{NiMnO}_6$ where ($x=0.0, 0.1, 0.2, 0.4, 0.6$).

Table 1. Structural Parameters of Double Perovskites $\text{La}_{2-x}\text{Sr}_x\text{NiMnO}_6$ ($x=0.0, 0.1, 0.2, 0.4$, and 0.6)

Sample	$x=0.0$	$x=0.1$	$x=0.2$	$x=0.4$	$x=0.6$
Structure	Monoclinic	Monoclinic	Monoclinic	Monoclinic	Monoclinic
Space Group	$P2_1/n$	$P2_1$	$P2_1$	$P2_1$	$P2_1$
a (Å)	5.46	5.44	5.44	5.46	5.17
b (Å)	5.52	5.49	5.64	5.46	5.82
c (Å)	7.72	7.76	7.72	7.97	7.96
V(Å ³)	232.8	231.4	236.6	237.4	239.2
β	90.41	90.86	90.73	92.63	92.32
GOF	1.02	0.93	1.00	0.98	0.82
R_p	11.39	12.93	13.27	12.28	12.13
R_{wp}	15.15	16.62	17.26	15.73	15.56
Crystallite size (nm)	46.36	37.88	30.38	34.87	31.37

the shifting of phonon-modes. In the intermediate frequency region above 200 cm^{-1} , five phonons ($\omega_{\text{TO}2}$ to $\omega_{\text{TO}6}$) were observed. This is because of the ions movement on B-site against (MnO_6) oxygen vibrations. The phonons $\omega_{\text{TO}3}$ and $\omega_{\text{TO}5}$ are missing for $x = 0.4$ and $x = 0.2$. In the higher frequency region above 400 cm^{-1} , we found two phonons ($\omega_{\text{TO}7}$ and $\omega_{\text{TO}8}$) which are associated to the stretching of phonon modes or octahedral distortion of MnO_6 . There is no phonon shifting found in $\omega_{\text{TO}2}$, $\omega_{\text{TO}4}$, $\omega_{\text{TO}6}$ and $\omega_{\text{TO}8}$. It is worth noticing that phonon $\omega_{\text{TO}7}$ which disappeared for $x=0.2$ and $x=0.6$ concentration, generate a new phonon $\omega_{\text{TO}8}$. The splitting of modes occurs in the range 171 - 259 cm^{-1} , due to structural distortions. For $x=0.2$, Sr has larger ionic radius as compared to La, this in turn increases the inter-ionic distance and force constant. It may be responsible for increase in oscillation strength of the phonon. Hence, because of this enhancement in distortion, phonons splitting take place. At $x=0.4$, four major phonons are observed. One of the phonons is little bit suppressed at that concentration, as shown in Figure 2 [25]. Optical phonon $\omega_{\text{TO}8}$ observed for $x = 0.0, 0.1, 0.2, 0.4, 0.6$ at high frequency value exhibited the structural distortion which is produced due to the substitution of Sr^{2+} . The complex part of the dielectric constant is used to measure conductivity by $\sigma_1(\omega)=\omega\epsilon_2/4\pi$ [26, 27]. The optical spectra of conductivity (Figure 3) of $\text{La}_{2-x}\text{Sr}_x\text{NiMnO}_6$ exhibit strong absorption peaks, which points out the semiconducting nature of $\text{La}_{2-x}\text{Sr}_x\text{NiMnO}_6$ as $\sigma(0)$ approaches zero. As strontium contents increase, these phonons shift towards higher frequency.

3.3 Electrical Properties

Temperature-dependent I-V curves within temperature range (303-423) K are shown in Figure 4. The current is increasing linearly both with increasing voltage and rise in temperature and thus, confirms the semiconducting behaviour of material. DC resistivity of Sr^{2+} doped double perovskites is shown in Figure 5. The resistivity of all the synthesised materials decreases with increase in temperature, again manifesting the semiconducting nature of the materials. This decrement in resistivity with respect to rise in temperature is due to the charges, which are thermally triggered due to conduction mechanism of hopping [28, 29]. The

activation energy of the material is obtained by the Arrhenius plot of $\ln(\rho)$ vs $1/K_B T$ in temperature range from 303 to 423 K. The equation used to calculate the activation energy is

$$\rho = \rho_0 \exp(E_a/K_B T) \quad (5)$$

Where T is temperature, “ ρ ” is the resistivity of sample, “ E_a ” is the activation energy and “ K_B ” is the Boltzmann constant. The slope of the graph of $\ln(\rho)$ vs $1/K_B T$, is the activation energy of individual samples. Inset graphs in Fig. 5 display the activation energy E_a for $\text{La}_{2-x}\text{Sr}_x\text{NiMnO}_6$ ($x=0.0, 0.1, 0.2, 0.4, 0.6$) and hence band gap energy is determined.

Generally, the band gap energy is more than 0.9 eV for the oxides of ionic conductors. If this energy is less than 0.2 eV then polaronic conduction occurs due to electrons (n-type) and if this energy is greater than 0.2eV then polaronic conduction occurs because of holes (p-type) [30]. In LSNMO, at $x = 0.0$ the polaronic conduction is of p-type. As we doped Sr ($x=0.1$) in LSNMO, we observed switching in polaronic conduction from p-type to n-type. For the Sr concentration up to $x = 0.4$, n-type polaronic conduction was observed. However, for $x = 0.6$, polaronic conduction switches again from p-type to n-type. For the validity of the polaronic conduction mechanism within the range of temperature 303 to 423K, we discussed the small polaron hopping (SPH) because band gap model is not enough to discuss the conduction mechanism. The small polaron hopping model is

$$\rho_{(t)}/T = \rho_a \exp(E_a/K_B T) \quad (6)$$

Where “ K_B ” Boltzmann constant, “T” is absolute temperature, E_a is the value of activation energy and ρ_a is the pre-fractional factor. In high temperature region, mostly the SPH mechanism is effective and Variable Range Hopping (VRH) mechanism is more dominant in the low temperature regime [31]. From Figure 6, it can be seen that the SPH model gives best linear fit to the results suggesting that our samples exhibit the SPH conduction.

3.4 Dielectric Properties

Figure 7 show that the undoped LNMO has a large value of dielectric constant at low frequency and high temperature. Figure 8 shows a similar trend

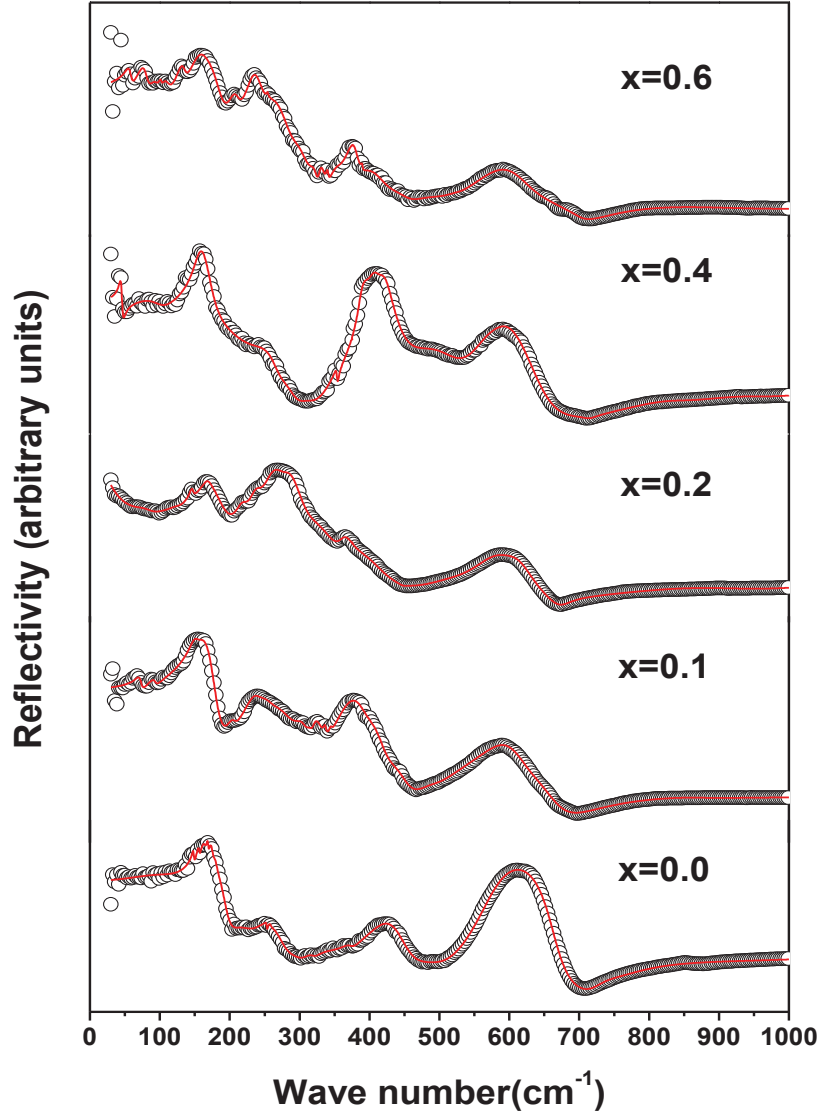


Fig. 2. IR reflectivity spectra for $\text{La}_{2-x}\text{Sr}_x\text{NiMnO}_6$ at room temperature where red lines denote the best fit to Lorentz Oscillator model and black circles show the experimental spectra.

Table 2. Transverse frequency of active IR phonon modes, and ϵ_∞ at room temperature.

Transverse frequency ($\omega_{\text{TO}i}$)	x =0.0	x =0.1	x =0.2	x =0.4	x =0.6
($\omega_{\text{TO}1}$)	155	151	146	159	160
($\omega_{\text{TO}2}$)	175	205	171	194	208
($\omega_{\text{TO}3}$)	253	237	237	—	235
($\omega_{\text{TO}4}$)	258	252	259	265	266
($\omega_{\text{TO}5}$)	319	323	—	356	340
($\omega_{\text{TO}6}$)	373	377	363	390	389
($\omega_{\text{TO}7}$)	430	407	—	425	—
($\omega_{\text{TO}8}$)	571	596	580	589	590
ϵ_∞	0.69	1.35	1.47	1.61	1.45

Table 3. Damping factor of active IR-phonon modes for $\text{La}_{2-x}\text{Sr}_x\text{NiMnO}_6$ ($x=0.0, 0.1, 0.2, 0.4, 0.6$)

Damping factor (γ_j)	x =0.0	x =0.1	x =0.2	x =0.4	x =0.6
γ_1	3	14	6	18	32
γ_2	10	14	51	153	20
γ_3	1	23	21	—	27
γ_4	4	36	36	40	58
γ_5	16	25	—	3	4
γ_6	17	53	24	12	17
γ_7	67	43	—	44	—
γ_8	75	75	68	52	101

Table 4. Oscillation strength of active IR-phonon modes for $\text{La}_{2-x}\text{Sr}_x\text{NiMnO}_6$ ($x=0.0, 0.1, 0.2, 0.4, 0.6$)

Oscillation strength (S_j)	x =0.0	x =0.1	x =0.2	x =0.4	x =0.6
S_1	0.03	0.25	0.16	4.51	1.32
S_2	0.19	0.05	3.90	7.3	0.24
S_3	0.00	0.16	0.57	—	0.64
S_4	0.00	0.29	2.05	0.73	1.10
S_5	0.01	0.24	—	0.01	0.01
S_6	0.02	0.74	0.09	0.63	0.01
S_7	0.60	0.15	—	0.3	—
S_8	0.62	0.39	0.32	0.09	0.60

for all Sr^{2+} doped double perovskites. It is seen that as temperature rises, the values of dielectric constant (ϵ') also enhanced in low frequency region. It is due to the fact that in low frequency region, dipoles try to align themselves in direction of applied AC electric field. In low frequencies, due to low oscillation in field, dipoles are able to align easily in the direction of the field and consequently, an increase in net polarisation is observed. Also at low value of frequency, high value of dielectric constants ascribed to grain boundaries defects and presence of vacancies of oxygen [28]. However, as frequency increases, the dielectric constant drops abruptly as the dipoles no longer follow the applied field frequency [31]. Accumulations of charges and dipoles contribution that are present near grain boundaries are responsible for the relaxation behaviour of dielectric materials [22]. The trend of

tangent loss ($\tan\delta$) with frequency and temperature for undoped LNMO is also shown in Figure 7. At low frequency, we examined high value of dissipation factor because of the presence of scattering of charges which are thermally triggered carriers and also due to lattice sites defects. Similar trend has been noticed in all Sr^{2+} doped double perovskites, which is shown in Fig. 9. Koop and Maxwell Wagner Model are used to describe the dielectric behaviour with respect to change in frequency [32]. This model explained that at lower frequency region, the dielectric medium contains grain boundaries which are poorly conducting but at higher frequency dielectric medium consist of grains that are highly conducting. At higher temperature, conductivity dominated and domain walls have a small contribution into tangent loss and result in increment in tangent loss[33].

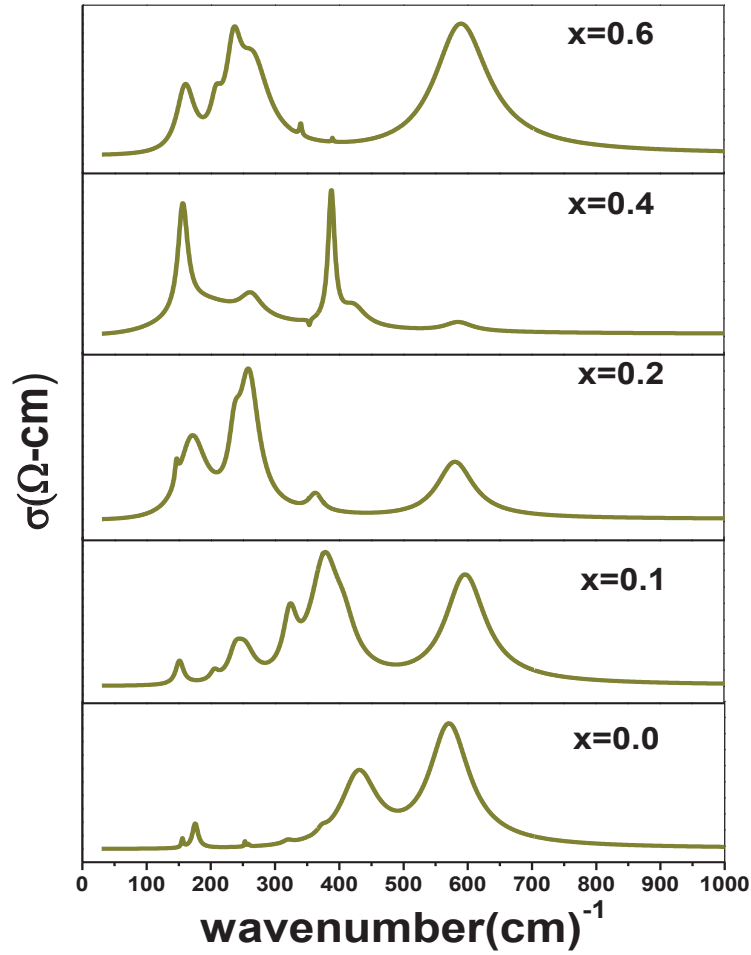
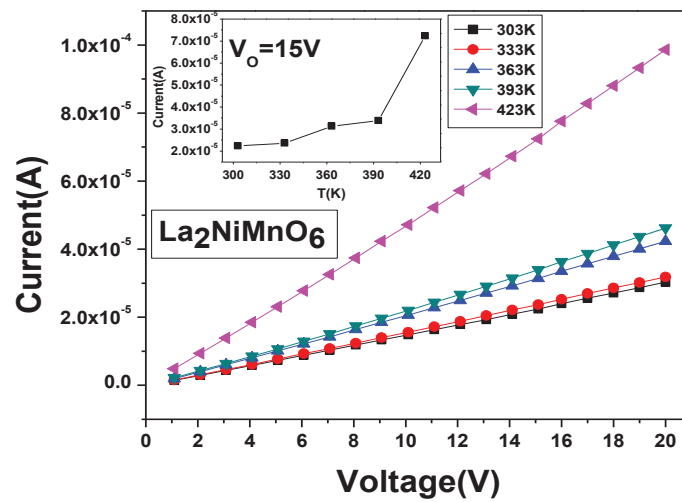


Fig. 3. Optical conductivity of $\text{La}_{2-x}\text{Sr}_x\text{NiMnO}_6$ ($x=0.0, 0.1, 0.2, 0.4, 0.6$)



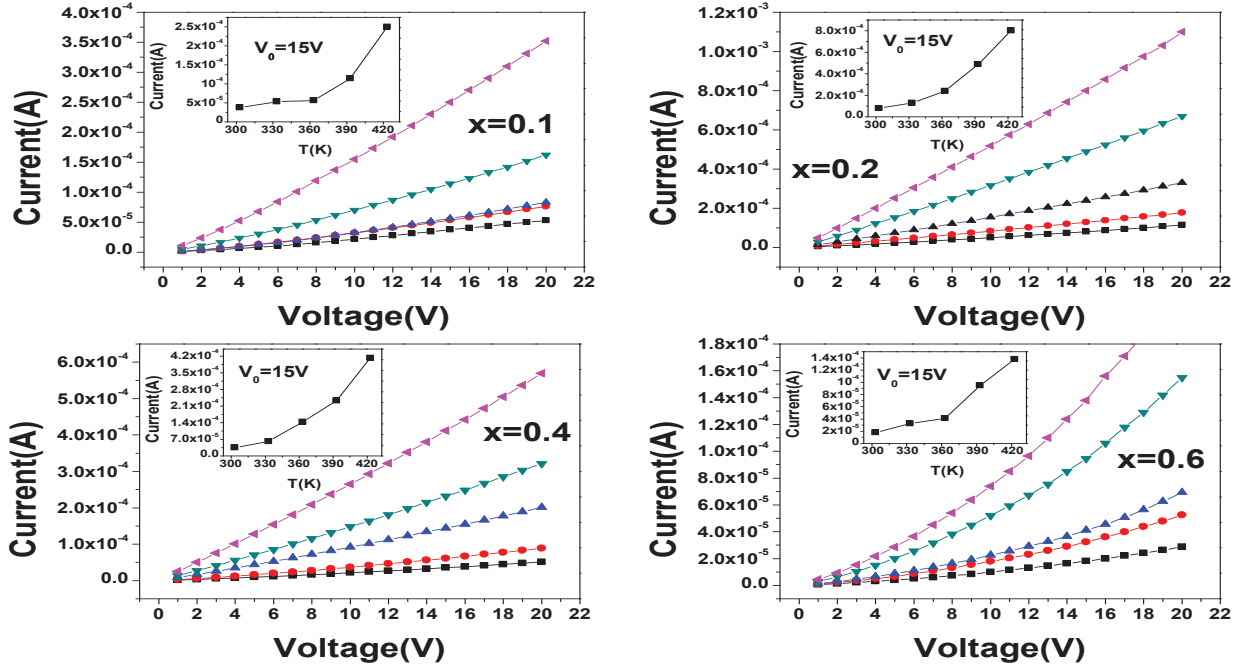


Fig. 4. Current vs. Voltage graphs at various temperature where temperature values are common in all graphs of $\text{La}_{2-x}\text{Sr}_x\text{NiMnO}_6$ ($x=0.0, 0.1, 0.2, 0.4, 0.6$) and inset graph at voltage 15V.

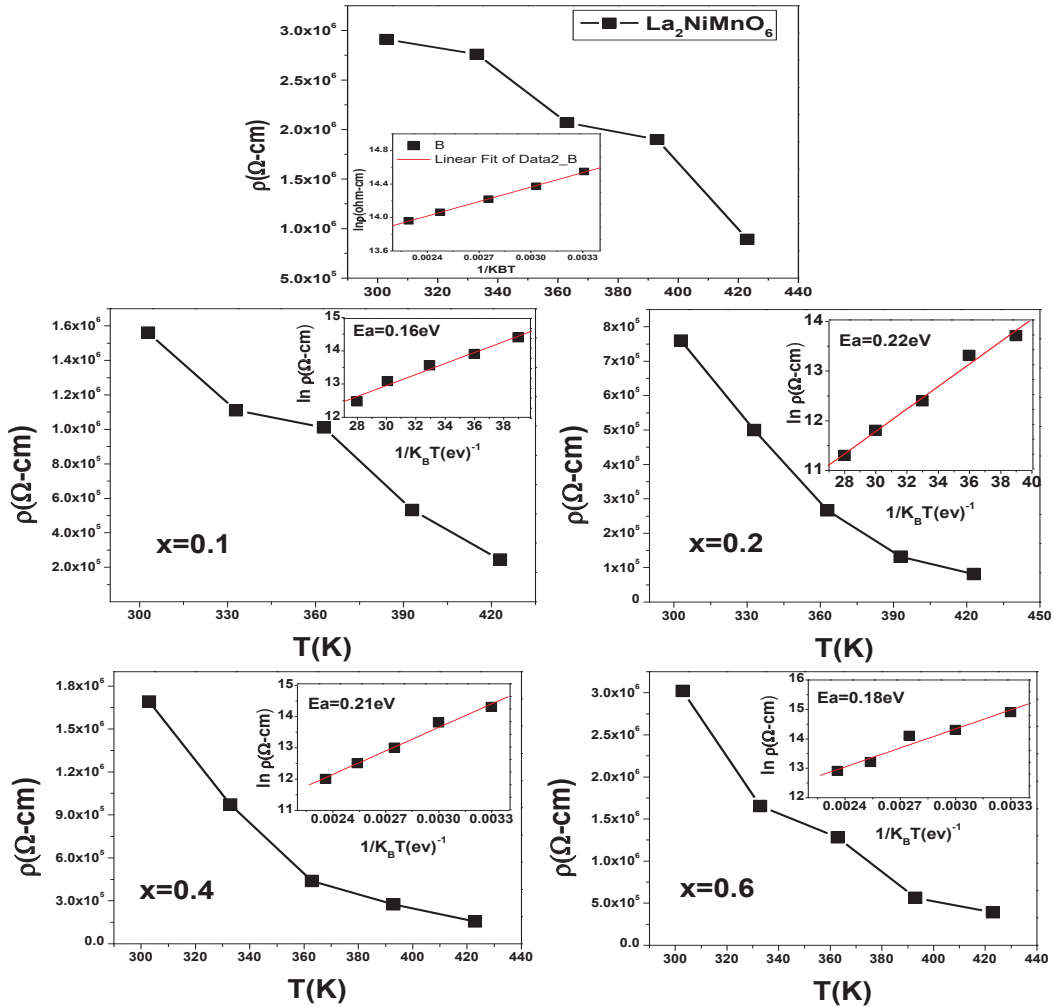


Fig. 5. Resistivity vs Temperature graphs of $\text{La}_{2-x}\text{Sr}_x\text{NiMnO}_6$ where ($x=0.0, 0.1, 0.2, 0.4, 0.6$); inset shows the results used to calculate activation energy.

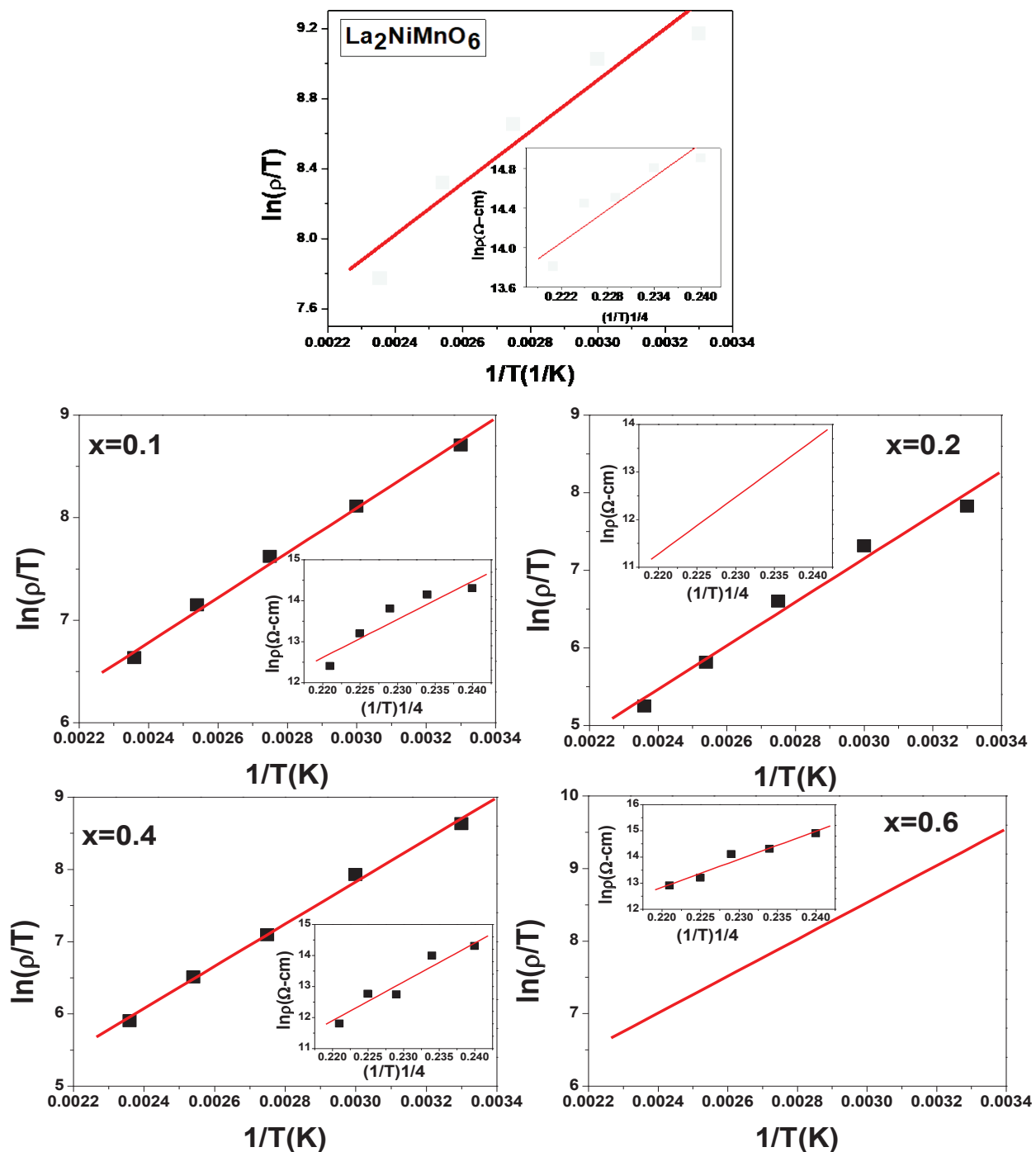


Fig. 6. Graph of $\ln(\rho/T)$ vs $1/T$ and inset shows $\ln\rho$ vs $(1/T)^{1/4}$ for LSNMO ($x=0.0, 0.1, 0.2, 0.4, 0.6$)

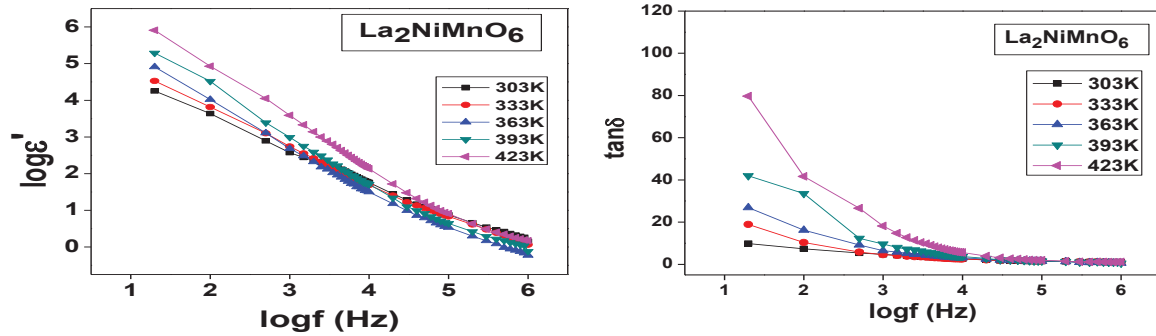


Fig. 7. Dielectric constant and loss tangent of $\text{La}_2\text{NiMnO}_6$

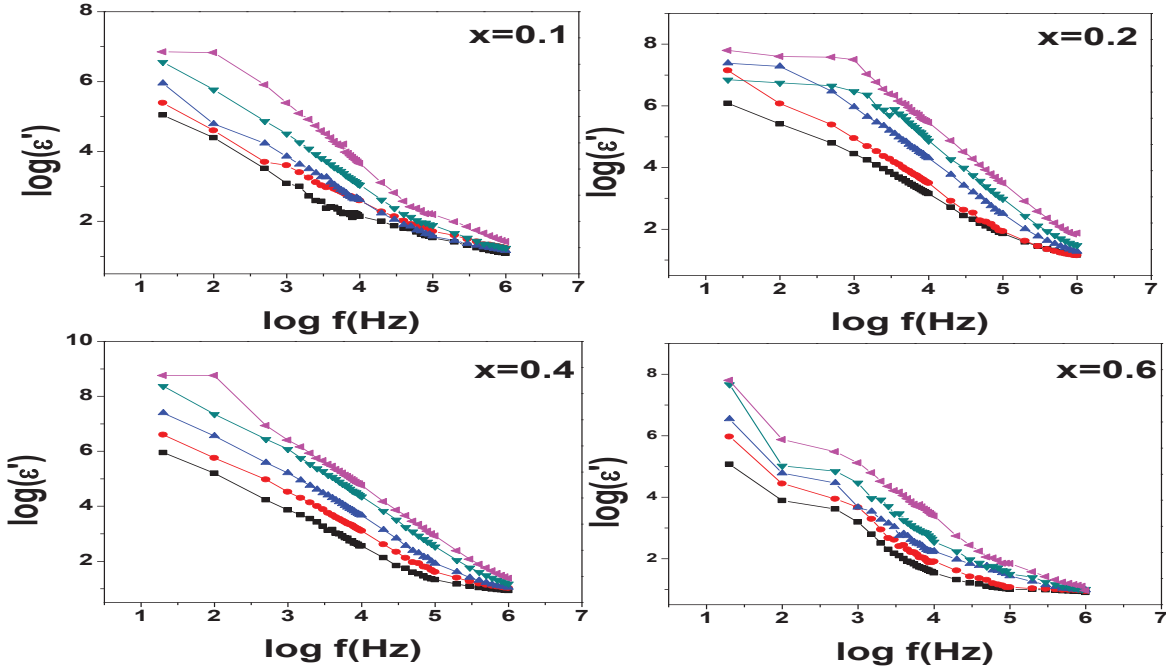


Fig. 8. Graph between $\log(\epsilon')$ vs $\log(f)$ for $\text{La}_{2-x}\text{Sr}_x\text{NiMnO}_6$ ($x=0.0, 0.1, 0.2, 0.4, 0.6$)

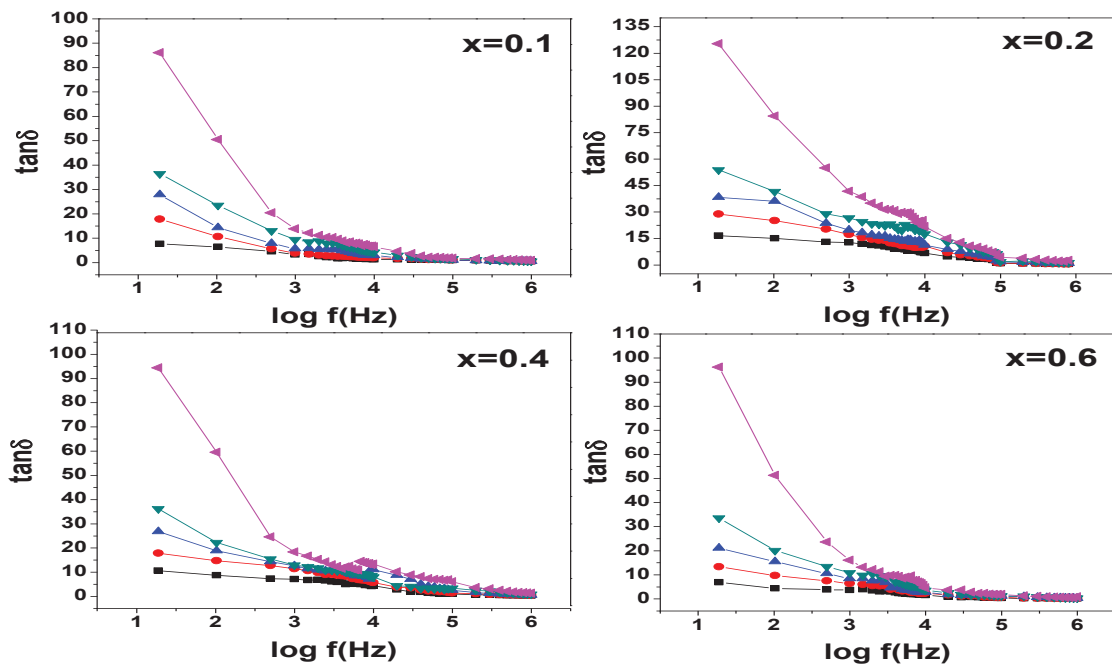


Fig. 9. Graphs between $\tan(\delta)$ vs $\log(f)$ for $\text{La}_{2-x}\text{Sr}_x\text{NiMnO}_6$ ($x=0.0, 0.1, 0.2, 0.4, 0.6$)

4. CONCLUSION

$\text{La}_{2-x}\text{Sr}_x\text{NiMnO}_6$ double perovskites with concentration ($x = 0.0, 0.1, 0.2, 0.4, 0.6$) were prepared by using sol-gel auto combustion technique. XRD technique was used to examine the structural properties and we found that all the samples with Sr doping have a monoclinic structure with space group $P2_1$ and $P2_1/n$ for $x=0.0$. The shift in frequency of the several observed phonons is associated with the doping of the Sr. Likewise, we have also found phonon modes splitting and suppression of peaks as we increase Sr concentration from $x=0.2$ to $x = 0.4$. Both the electrical and dielectric properties confirm semiconducting behaviour; a decrease in activation energy with an increase in the concentration of Sr has been found; and the multiferroics seem to exhibit the SPH conduction mechanism.

5. CONFLICT OF INTEREST

The author declares no conflict of interest.

6. REFERENCES

1. S. Aarif Ul Islam and M. Ikram, Structural stability improvement, Williamson Hall analysis and band-gap tailoring through A-site Sr doping in rare earth based double perovskite $\text{La}_2\text{NiMnO}_6$, *Rare Metals* 38 (9), 805-813 (2019).
2. T. Kimura, S. Kawamoto, I. Yamada, M. Azuma, M. Takano and Y. Tokura, Magnetocapacitance effect in multiferroic BiMnO_3 , *Physical Review B* 67 (18), 180401-180409 (2003).
3. G. Lawes, A. P. Ramirez, C. M. Varma and M. A. Subramanian, Magnetodielectric Effects from Spin Fluctuations in Isostructural Ferromagnetic and Antiferromagnetic Systems, *Physical Review Letters* 91 (25), 257208-257217 (2003).
4. K. Kuepper, M. Kadiroglu, A. V. Postnikov, K. C. Prince, M. Matteucci, V. R. Galakhov, H. Hesse, G. Borstel and M. Neumann, Electronic structure of highly ordered $\text{Sr}_2\text{FeMoO}_6$: XPS and XES studies, *Journal of Physics: Condensed Matter* 17 (27), 4309-4317 (2005).
5. U. Lüders, M. Bibes, K. Bouzehouane, E. Jacquet, J. P. Contour, S. Fusil, J. F. Bobo, J. Fontcuberta, A. Barthélémy and A. Fert, Spin filtering through ferrimagnetic NiFe_2O_4 tunnel barriers, *Applied Physics Letters* 88 (8), 082505 (2006).
6. M. Gajek, M. Bibes, A. Barthélémy, K. Bouzehouane, S. Fusil, M. Varela, J. Fontcuberta and A. Fert, Spin filtering through ferromagnetic BiMnO_3 tunnel barriers, *Physical Review B* 72 (2), 020406-020415 (2005).
7. K. I. Kobayashi, T. Kimura, H. Sawada, K. Terakura and Y. Tokura, Room-temperature magnetoresistance in an oxide material with an ordered double-perovskite structure, *Nature* 395 (6703), 677-680 (1998).
8. R. Palai, R. S. Katiyar, H. Schmid, P. Tissot, S. J. Clark, J. Robertson, S. A. T. Redfern, G. Catalan and J. F. Scott, β phase and γ - β metal-insulator transition in multiferroic BiFeO_3 , *Physical Review B* 77 (1), 014110-014118 (2008).
9. P. Monthoux, D. Pines and G. G. Lonzarich, Superconductivity without phonons, *Nature* 450, 1177 (2007).
10. M. Imada, A. Fujimori and Y. Tokura, Metal-insulator transitions, *Reviews of Modern Physics* 70 (4), 1039-1263 (1998).
11. M. T. Anderson, K. B. Greenwood, G. A. Taylor and K. R. Poeppelmeier, B-cation arrangements in double perovskites, *Progress in Solid State Chemistry* 22 (3), 197-233 (1993).
12. V. Cuartero, J. Blasco, J. García, S. Lafuerza, G. Subías, J. A. Rodriguez-Velamazán and C. Ritter, Enhancement of ferromagnetic correlations on multiferroic TbMnO_3 by replacing Mn with Co, *Journal of Physics: Condensed Matter* 24 (45), 455601 (2012).
13. J. Ahmad, M. Usman and U. Nissar, Effect of Yttrium doping on structural, optical and transport properties of $\text{La}_2\text{NiMnO}_6$, *Materials Research Express* 6 (12), 125706 (2019).
14. L. Guo, Y. Bai, C. Huang and W. Ma, Revisiting La_2MMnO_6 (M= Co, Ni, Cu, Zn) perovskites in view of 3d-electron configuration, *Journal of Applied Physics* 124 (6), 065103 (2018).
15. R. I. Dass, J. Q. Yan and J. B. Goodenough, Oxygen stoichiometry, ferromagnetism, and transport properties of $\text{La}_{2-x}\text{NiMnO}_6 + \delta$, *Physical Review B* 68 (6), 064415 (2003).
16. J. B. Goodenough, 1962.
17. Y. Q. Lin, X. M. Chen and X. Q. Liu, Relaxor-like dielectric behavior in $\text{La}_2\text{NiMnO}_6$ double perovskite ceramics, *Solid State Communications* 149 (19), 784-787 (2009).
18. K. Asai, H. Sekizawa and S. Iida, Magnetisation measurements and ^{55}Mn NMR studies of $\text{LaNiO}_{1-x}\text{MnO}_x$, *Journal of the Physical Society of Japan* 47 (4), 1054-1060 (1979).
19. R. J. Booth, R. Fillman, H. Whitaker, A. Nag, R.

- M. Tiwari, K. V. Ramanujachary, J. Gopalakrishnan and S. E. Lofland, An investigation of structural, magnetic and dielectric properties of R_2NiMnO_6 (R=rare earth, Y), *Materials Research Bulletin* 44 (7), 1559-1564 (2009).
20. E. K. H. Salje, M. F. Osmaston, R. K. Nions, R. Clayton and B. Parsons, Characteristics of perovskite-related materials, *Philosophical Transactions of the Royal Society of London. Series A, Mathematical and Physical Sciences* 328 (1599), 409-416 (1989).
21. R. P. Maiti, S. Dutta, M. Mukherjee, M. K. Mitra and D. Chakravorty, Magnetic and dielectric properties of sol-gel derived nanoparticles of double perovskite Y_2NiMnO_6 , *Journal of Applied Physics* 112 (4), 044311-044319 (2012).
22. R. C. Sahoo, S. Das and T. K. Nath, Effect of rare earth site substitution on magnetic and transport properties of Ln_2CoMnO_6 ($Ln = La, Sm$ and Gd) double perovskites, *Journal of Magnetism and Magnetic Materials* 460, 409-417 (2018).
23. J. Ahmad, U. Ahmad and S. H. Bukhari, Synthesis and optical properties of $La_{1-x}Ce_xMnO_3$ studied by infrared reflectivity measurements, *Chinese Journal of Physics* 56 (4), 1439-1448 (2018).
24. J. Ahmad, H. Yamanaka and H. Uwe, Bismuth charge disproportionation in semiconducting $BaPb_xBi_{1-x}O_3$ studied by infrared reflection spectroscopy, *Journal of Physics: Condensed Matter* 19 (26), 266223-266230 (2007).
25. I. Terasaki, T. Nakahashi, A. Maeda and K. Uchinokura, Optical study of the doping effect in the metallic oxide $(Nd,Sr)CoO_3$, *Physical Review B* 43 (1), 551-554 (1991).
26. D. R. Patil and B. K. Chougule, Effect of resistivity on magnetoelectric effect in $(x)NiFe_2O_4-(1-x)Ba_{0.9}Sr_{0.1}TiO_3$ ME composites, *Journal of Alloys and Compounds* 470 (1), 531-535 (2009).
27. M. Idrees, M. Nadeem and M. M. Hassan, Investigation of conduction and relaxation phenomena in $LaFe_{0.9}Ni_{0.1}O_3$ by impedance spectroscopy, *Journal of Physics D: Applied Physics* 43 (15), 155401-155408 (2010).
28. J. P. Palakkal, C. R. Sankar, A. P. Paulose and M. R. Varma, Hopping conduction and spin glass behavior of La_2FeMnO_6 , *Journal of Alloys and Compounds* 743, 403-409 (2018).
29. J. A. Khan and J. Ahmad, Double perovskite La_2CrMnO_6 : synthesis, optical and transport properties, *Materials Research Express* 6 (11), 115906-115918 (2019).
30. M. S. Khandekar, R. C. Kambale, J. Y. Patil, Y. D. Kolekar and S. S. Suryavanshi, Effect of calcination temperature on the structural and electrical properties of cobalt ferrite synthesised by combustion method, *Journal of Alloys and Compounds* 509 (5), 1861-1865 (2011).
31. D. Singh and A. Mahajan, Effect of A-site cation size on the structural, magnetic, and electrical properties of $La_{1-x}Nd_xMn_{0.5}Cr_{0.5}O_3$ perovskites, *Journal of Alloys and Compounds* 644, 172-179 (2015).
32. C. G. Koops, On the Dispersion of Resistivity and Dielectric Constant of Some Semiconductors at Audiofrequencies, *Physical Review* 83 (1), 121-124 (1951).
33. H. Das, U. V. Waghmare, T. Saha-Dasgupta and D. D. Sarma, Theoretical evidence and chemical origin of the magnetism-dependent electrostructural coupling in La_2NiMnO_6 , *Physical Review B* 79 (14), 144403-144409 (2009).

